Bond-order potential for magnetic body-centered-cubic iron and its transferability

Yi-Shen Lin,[1] M. Mrovec,[2] and V. Vitek[1,*]

[1]*Department of Materials Science and Engineering, University of Pennsylvania, 3231 Walnut Street, Philadelphia, Pennsylvania 19104, USA*

[2]*Fraunhofer Institute for Mechanics of Materials IWM, Wöhlerstraße 11, 79108 Freiburg, Germany and Institute of Applied Materials - Computational Materials Science (IAM-CMS), Karlsruhe Institute of Technology, Engelbert-Arnold-Straße 4, 76131 Karlsruhe, Germany*

(Received 10 December 2015; revised manuscript received 3 March 2016; published 14 June 2016)

We derived and thoroughly tested a bond-order potential (BOP) for body-centered-cubic (bcc) magnetic iron that can be employed in atomistic calculations of a broad variety of crystal defects that control structural, mechanical, and thermodynamic properties of this technologically important metal. The constructed BOP reflects correctly the mixed nearly free electron and covalent bonding arising from the partially filled *d* band as well as the ferromagnetism that is actually responsible for the stability of the bcc structure of iron at low temperatures. The covalent part of the cohesive energy is determined within the tight-binding bond model with the Green's function of the Schrödinger equation determined using the method of continued fractions terminated at a sufficient level of the moments of the density of states. This makes the BOP an O(N) method usable for very large numbers of particles. Only *dd* bonds are included explicitly, but the effect of *s* electrons on the covalent energy is included via their screening of the corresponding *dd* bonds. The magnetic part of the cohesive energy is included using the Stoner model of itinerant magnetism. The repulsive part of the cohesive energy is represented, as in any tight-binding scheme, by an empirical formula. Its functional form is physically justified by studies of the repulsion in face-centered-cubic (fcc) solid argon under very high pressure where the repulsion originates from overlapping *s* and *p* closed-shell electrons just as it does from closed-shell *s* electrons in transition metals squeezed into the ion core under the influence of the large covalent *d* bonding. Testing of the transferability of the developed BOP to environments significantly different from those of the ideal bcc lattice was carried out by studying crystal structures and magnetic states alternative to the ferromagnetic bcc lattice, vacancies, divacancies, self-interstitial atoms (SIAs), paths continuously transforming the bcc structure to different less symmetric structures and phonons. The results of these calculations are compared with either experiments or calculations based on the density functional theory (DFT), and they all show very good agreement. Importantly, the lowest energy configuration of SIAs agrees with DFT calculations that show that it is an exception within bcc transition metals controlled by magnetism. Moreover, the migration energy of interstitials is significantly lower than that of vacancies, which is essential for correct analysis of the effects of irradiation. Finally, the core structure and glide of $\frac{1}{2}\langle 111\rangle$ screw dislocations that control the plastic flow in single crystals of bcc metals was explored. The results fully agree with available DFT based studies and with experimental observations of the slip geometry of bcc iron at low temperatures.

DOI: 10.1103/PhysRevB.93.214107

I. INTRODUCTION

Computer simulations have become one of the major methodologies for studying structural, thermodynamic, and other properties of crystal defects, including their role in various physical and mechanical properties of materials. In particular, investigations of extended defects, such as dislocations, grain and phase boundaries, nanovoids, or cracks have been very widespread, owing to the important role these defects play in a broad variety of properties of crystalline materials. An obvious precursor for such calculations is a physically justified description of interatomic interactions in the system studied. The present state of the art calculations are based on the density functional theory (DFT), and if every calculation could be carried out in this way there would be no need for further elaboration on interatomic interactions. However, this is not the case, owing to rather stringent limitations on the number of particles that can be used in DFT calculations and, most importantly, the three-dimensional periodic boundary conditions required in practically all the available DFT codes [1]. This problem can be circumvented by coarse graining the electronic structure that determines the cohesion into interatomic potentials describing interactions between atoms [2]. The crucial property of such potentials is that they must comprise all the essential aspects of the cohesion. In the case of transition metals, it means that such potentials reflect correctly the mixed nearly free electron and covalent bonding arising from the partially filled *d* band [3]. This also applies to iron, but an additional important aspect is the ferromagnetism that is actually responsible for the stability of the body-centered-cubic (bcc) structure of iron (α-iron) at low temperatures [4].

In this paper, we present the bond-order potential (BOP) for iron together with a detailed testing of its transferability to environments very different from that of the equilibrium bcc lattice. Iron is indubitably one of the technologically most important metals involved in a broad variety of structural applications. Hence, atomic level investigation of the mechanical behavior of iron and its alloys is of paramount importance and has been pursued over many years using various interatomic potentials. First were pair potentials (e.g.,

*vitek@seas.upenn.edu

Ref. [5]), and in more recent years central-force potentials of the embedded atom method (EAM) or Finnis-Sinclair (F-S) type were advanced (e.g., Refs. [6] and [7]). None of these interatomic potentials includes an appropriate description of directional bonding of covalent type arising from the partially filled d band. Bond directionality has been included empirically in the modified EAM [8], and it is automatically a part of the empirical potentials proposed in Ref. [9] and discussed recently in Ref. [10] that employ the functional form originally developed by Tersoff for Si [11]. These potentials do not include any interactions arising from ferromagnetism, and the only attempt to include magnetic effects into the central force F-S type potential was made in Ref. [12]. The only potential that includes both the directionality of bonding and magnetism in iron is the BOP proposed in Ref. [13]. The potential presented in this paper is a significant enhancement of this model. It employs the same approach when treating the ferromagnetism, namely the Stoner model [14,15], but augments considerably the description of bonding arising from the partially filled d band and includes the effect of s electrons on the d bonds. Similarly, the repulsion between atoms, represented in Ref. [13] by a pair potential, is significantly upgraded by including its dependence on the local atomic environment, which allows exact reproduction of all three cubic elastic moduli when parameterizing the potential. The only empirical data in this development are the cohesive energy, the lattice parameter, and three second order elastic moduli of the ideal bcc lattice. These are used when determining the coefficients of the functional form describing repulsion between atoms. No empirical data have been employed in the development of both the attractive covalent part of the energy and the magnetic contribution, but some parameters in these parts of the cohesive energy have been obtained from DFT calculations.

The paper is organized as follows. In Sec. II, we describe in some detail the attractive covalent part of the cohesive energy arising from the partially filled d band and the magnetic contribution, as well as the repulsive part of the cohesive energy. The important aspect of the covalent part is inclusion of the effect of s electrons into the calculations in which only dd bonds are involved explicitly. In the repulsion, the most important aspect is that it consists of a combination of environment dependent central force term and a pair potential. In Sec. III, we present an extensive investigation of the transferability of the developed BOP. This involves study of crystal structures and magnetic states alternative to the ferromagnetic (FM) bcc lattice, vacancies, divacancies, self-interstitials, paths continuously transforming the bcc structure to different less symmetric structures, phonons, and atomistic modeling of the structure and glide of $\frac{1}{2}\langle 111\rangle$ screw dislocations that dominate the plastic deformation of single crystals of all bcc metals.

II. DEVELOPMENT OF THE BOP

The general theory of BOPs, originally advanced by Pettifor and co-workers [16–18], has been elucidated in several recent reviews [19–24]. Hence, we summarize only briefly the main aspects, in particular those important for the bcc iron.

Within BOPs the cohesive energy of the bcc FM iron is written as

$$E^{\mathrm{coh}} = E^{\mathrm{cov}} + E^{\mathrm{mag}} + E^{\mathrm{rep}}. \tag{1}$$

The covalent energy arising owing to the partially filled d band is [25]

$$E^{\mathrm{cov}} = \sum_{\sigma=\uparrow,\downarrow} \sum_{i,\alpha} \sum_{j\neq i,\beta} \rho^{\sigma}_{i\alpha,j\beta} H^{\sigma}_{j\beta,i\alpha}, \tag{2}$$

where $\rho^{\sigma}_{i\alpha,j\beta}$ is the density matrix element for the bond between the orbital α centered at atom i and the orbital β centered at atom j, and $H^{\sigma}_{j\beta,i\alpha}$ is the corresponding element of the Hamiltonian matrix; σ represents the two possible spin states. In the development of BOPs for transition metals, only dd bonds are included explicitly (see the above mentioned reviews and Ref. [26]). Using the Slater-Koster [27] analysis, the Hamiltonian elements are expressed via bond angles and corresponding bond integrals (BIs). The E^{mag} is treated within the Stoner model of itinerant magnetism [15] introduced to the development of BOPs in Ref. [25]; it is discussed in more detail below. The repulsive part of the cohesive energy comprises two contributions, a pairwise interaction (E^{pair}) and an environment dependent central force contribution (E^{env}), using the same approach as in Ref. [26] and also summarized below.

A. Covalent part of the cohesive energy: E^{cov}

The BIs and their dependence on the interatomic distance, R_{ij}, between atoms i and j were obtained from DFT calculations via a projection scheme [28,29]. In this scheme, the DFT calculations are first performed for a variety of atomic configurations (several diverse crystal structures and volumes) that correspond to different bonding environments and material densities. Subsequently, a minimal basis of atomic orbitals (AOs) is constructed such as to give the best representation of the wave functions found in the DFT calculations. The Slater-Koster two-center BIs are then obtained using this basis of the AOs and the Hamiltonian obtained from the self-consistent DFT calculations. The dd BIs as functions of interatomic separation R, obtained from the orthogonalized s and d basis, are shown in Fig. 1 as empty circles. The important feature is that different values of BIs, in particular $dd\pi$ and $dd\delta$, are found for the same interatomic spacing attained in calculations for bcc lattices with different densities as the separation of the nearest

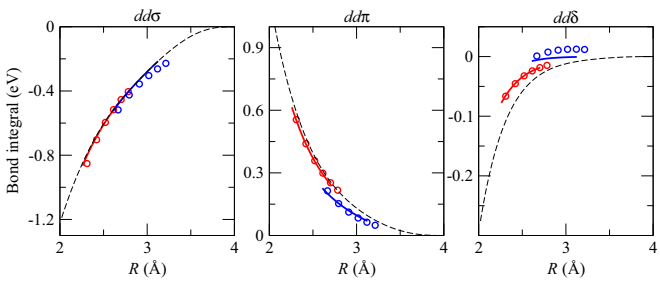

FIG. 1. BIs used in BOPs for bcc Fe. Circles: BIs determined from the sd basis of AOs and the Hamiltonian obtained from the self-consistent DFT calculations. Solid lines: screened BIs calculated according to Eq. (3). Dashed lines: $\beta_\tau(R_{ij})$, given by Eq. (A1). The red and blue colors correspond to R from regions of the first and second nearest neighbors in bcc lattices of different densities.

(red) or the second nearest neighbors (blue), respectively. This non-uniqueness of the R dependence of BIs, which manifests itself as discontinuities, results from the environmental dependence of BIs. Such discontinuities, found also in earlier studies [30,31], originate from screening effects of electrons/orbitals (primarily of s type) associated with atoms neighboring the dd bond considered. Instead of including explicitly the full sd basis, this effect can be taken into account implicitly via screening of the dd BIs, as proposed in Ref. [32]. The screened dd BIs of the type τ, where $\tau = \sigma, \pi$, or δ, are then

$$\widetilde{\beta}_{\tau}^{ij} = \beta_{\tau}(R_{ij})\big(1 - S_{\tau}^{ij}\big), \tag{3}$$

where R_{ij} is the separation of atoms i and j, S_{τ}^{ij} is the screening function, and $\beta_{\tau}(R_{ij})$ is the unscreened BI. A detailed description of these quantities is presented in Appendix A [33].

A crucial requirement imposed in both the development and use of BOPs is the condition of the local charge neutrality (LCN), which is a sensible constraint for metals where any charge variation is rapidly screened. This condition is written as

$$\sum_{\alpha}\left(\sum_{\sigma=\uparrow,\downarrow}\rho_{i\alpha,i\alpha}^{\sigma} - N_{i\alpha}^{\mathrm{atom}}\right) = 0, \tag{4}$$

where $N_{i\alpha}^{\mathrm{atom}}$ is the occupancy of the atomic-like orbital $|i\alpha\rangle$ in the free atom. The number of d electrons on every atom ($N_d = \sum_{\alpha} N_{i\alpha}^{\mathrm{atom}}$) is set to 7.1 (the same as in Ref. [13]), which is a reasonable value considering that the electronic configuration of an isolated Fe atom is [Ar] $3d^6\ 4s^2$. The LCN is attained in calculations by adjusting self-consistently the diagonal elements of the Hamiltonian, $H_{i\alpha,i\alpha}^{\sigma} = \varepsilon_{i\alpha}^{\sigma}$. As explained below, this is done in conjunction with the self-consistent adjustment of the magnetic moment associated with the atom i. In order to smear the sharp cutoff of the energy at the Fermi level and to damp down the associated long-range Friedel oscillations, a fictitious electronic temperature (T_f) is introduced [34]; as in the previous paper [13], we set $k_{\mathrm{B}}T_{\mathrm{f}} = 0.1\mathrm{eV}$, where k_{B} is the Boltzmann's constant. This method increases the rate of the convergence of both the energy and forces when employing BOPs.

Within the BOP scheme, the density matrix $\rho_{i\alpha,j\beta}^{\sigma}$ is determined by employing the expansion of the local density of states into its moments [35] and using the method of continued fractions for the Green's function of the Schrödinger equation [36–38]. The continued fractions were limited to nine moments of the local density of states, which was found in previous studies to reproduce the density of states with a satisfactory accuracy when compared to full tight-binding (TB) calculations [13,30,31]. The limitation to the finite number of moments of the density of states is the reason that BOPs are an O(N) method while full TB is an O(N^3) method. The algorithms for evaluation of the Green's function elements are implemented in the Oxford order-N package (OXON) [17,18,39] that has been used in both the development and application of BOPs.

B. Magnetic part of the cohesive energy: E^{mag}

Within the Stoner model, different collinear magnetic states, up and down spins of electrons, are introduced via different on-site energies, $\varepsilon_{i\alpha}^{\uparrow,\downarrow}$, corresponding to two possible spin states. Since only d electrons are included explicitly in the BOPs for iron, the corresponding diagonal elements of the Hamiltonian are [25]

$$\varepsilon_{id}^{\uparrow,\downarrow} = \varepsilon_{id}^{0} \pm \tfrac{1}{2} I m_i, \tag{5}$$

where m_i is the magnitude of the difference in the number of d electrons on site i with spin parallel and antiparallel to the local magnetic moment, I is the Stoner exchange integral, and $+$ and $-$ correspond to spin antiparallel ($\uparrow$) and parallel ($\downarrow$) to the local magnetic moment at site i, respectively. We use $I = 0.8\,\mathrm{eV}$ as in Ref. [13], where I was first obtained on the basis of DFT calculations but slightly readjusted to attain a correct magnetic behavior within the d-only model. The local exchange splitting on atom i, $\Delta_i = I m_i$, is determined self-consistently from calculations of the number of up and down electronic spins for each site using the spin-polarized version of the method of continued fractions for the Green's function of the Schrödinger equation when evaluating the density matrix $\rho_{i\alpha,j\beta}^{\sigma}$. The magnetic contribution to the energy is then [25]

$$E^{\mathrm{mag}} = -\frac{1}{4}\sum_{i} I\big(m_i^2 - m_{\mathrm{atom}}^2\big), \tag{6}$$

where m_{atom} is the magnetic moment of the free atom. Furthermore, the LCN condition [Eq. (4)] has to be satisfied concomitantly, and since the diagonal Hamiltonian elements contain m_i [Eq. (5)] both the self-consistency of the local exchange splitting and charge neutrality have to be attained concurrently. The corresponding algorithms are all implemented in the OXON package.

C. Repulsive part of the cohesive energy: E^{rep}

In any version of TB, and therefore also in BOPs, the repulsive part of the cohesive energy is not derived rigorously using a quantum mechanical treatment. Instead, it is formulated empirically by fitting a physically justified functional form to reproduce the experimental and/or DFT-calculated values of some basic properties of the materials studied. In the current development, we follow the same route as in the case of nonmagnetic (NM) transition metals, presented in more detail in Ref. [26]. In this case,

$$E^{\mathrm{rep}} = E^{\mathrm{env}} + E^{\mathrm{pair}}. \tag{7}$$

Both parts of E^{rep} depend only on the separation of particles, but E^{env} has a many-body character while E^{pair} is a pairwise repulsion. Our conjecture is that the functional form for E^{env} is analogous to that proposed by Aoki and Kurokawa [40] in their study of the repulsion in face-centered-cubic (fcc) solid argon under very high pressure that originates from overlapping of s and p closed-shell electrons. The physical reason is that, in transition metals, including iron, E^{env} also arises from the overlap repulsion of s electrons that are squeezed into the ion core regions under the influence of the large covalent d-bonding forces [41]. The adjustable parameters in both E^{env} and E^{pair} are determined such that the resulting BOP reproduces exactly the experimental values of the lattice constant, cohesive energy, and three elastic constants

(C_{11}, C_{12}, and C_{44}) of the equilibrium bcc iron. Details of evaluation of E^{env} and E^{pair} are presented in Appendix B.

While both E^{cov} and E^{mag} contribute to the Cauchy pressure, their contribution is not equal to its experimental value ($1/2[C_{12} - C_{44}]$). However, the presence of the environmental dependence allows us to attain the experimental value of the Cauchy pressure by fitting fully the elastic moduli. The same cannot be achieved using a pairwise potential only since this does not contribute to the Cauchy pressure [42,43]. In the earlier development [13], only a repulsive pair potential was used, and thus the Cauchy pressure was not fully reproduced.

D. Determination of the force on an atom

The force on an atom k, $\mathbf{F}_k = -\text{grad}_{\mathbf{r}_k} E^{\text{coh}}$. As shown in previous studies (see reviews in Refs. [19–22]), the force arising from E^{cov} can be determined to a good approximation using the Hellmann-Feynman theorem [44]. Moreover, it was proved in Refs. [25] and [45] that the force arising from E^{mag}, treated within the Stoner model, can also be included into the Hellmann-Feynman type expression so that

$$\mathbf{F}_k^{\text{cov+mag}} = -\sum_{\sigma=\uparrow,\downarrow} \sum_{i\alpha \neq j\beta} \rho^{\sigma}_{i\alpha,j\beta} \text{grad}_{\mathbf{r}_k}(H^{\sigma}_{j\beta,i\alpha}). \quad (8a)$$

Thus, there is no force arising independently from E^{mag}, but, of course, the effect of local self-consistent magnetic moments is concealed in $\rho^{\sigma}_{i\alpha,j\beta}$. The force arising from the repulsive term is simply

$$\mathbf{F}_k^{\text{rep}} = -\text{grad}_{\mathbf{r}_k}(E^{\text{rep}}). \quad (8b)$$

III. TESTING OF TRANSFERABILITY OF THE DEVELOPED BOP FOR BCC IRON

The main purpose of the developed BOP is to investigate structures and properties of atomic ensembles that deviate significantly from the ideal bcc lattice. Specifically, these are centers of crystal defects, in particular the extended ones such as dislocations, grain boundaries, and other interfaces. Obviously, the crucial requirement for such demanding studies is the capability of the BOP model to describe accurately distorted environments far away from equilibrium. While this can never be guaranteed unequivocally, a thorough testing of the transferability involving a variety of atomic environments that differ significantly from the equilibrium bcc lattice enhances considerably our confidence in employing the BOPs. For this purpose, we investigate the energy of lattice structures other than the bcc lattice, including alternate magnetic states, the energy variation when the bcc lattice is deformed along several transformation paths [46,47], formation energies of vacancies, divacancies, and self-interstitial atoms (SIAs), phonon spectra, and γ surface for $\{101\}$ planes, which relates to the core structure of $1/2\langle 111\rangle$ screw dislocations that govern the plastic deformation of bcc metals [48,49]. Results of these tests can be compared with those obtained by DFT calculations or appropriate experiments.

A. Alternate crystal structures and magnetic states

The structures investigated are bcc, fcc, and hexagonal close packed (hcp), each with three possible magnetic states, namely NM, FM, and antiferromagnetic (AFM). The results are summarized in Table I, which shows that the state with the lowest energy is FM bcc. Importantly, in the NM state, the fcc and hcp lattices are more stable than the bcc lattice. Moreover, using the developed BOP we calculated the elastic moduli for the NM bcc state and found that the shear modulus $1/2(C_{11}-C_{12})$ is negative; the shear modulus C_{44} is positive. This implies that the NM state is not only a high energy state but is in fact unstable.

TABLE I. Equilibrium energies (meV atom^{-1}) of bcc, fcc, and hcp structures in different magnetic states relative to that of FM bcc structure. All structures were relaxed with respect to the corresponding lattice parameter.

	FM	AFM	NM
bcc	0	431	498
fcc	99	271	339
hcp	97	197	331

This demonstrates that introducing magnetism into the BOP for Fe is crucial for attaining the correct ground state, namely FM bcc (see Ref. [4], which proves that the ferromagnetism stabilizes the bcc structure of iron at low temperatures). We have also compared the energy versus atomic volume dependences calculated using the BOPs to the results of the DFT calculations carried out in Ref. [50]. These results are presented in Fig. 2, and it is seen that the BOP results are in an excellent agreement with the DFT calculation.

B. Vacancies and divacancies

A supercell of dimensions $3a \times 3a \times 3a$, where a is the equilibrium lattice parameter, was used, and the atomic arrangement was always fully relaxed. Table II compares the formation energies of vacancies and divacancies obtained by the BOP with DFT calculations [51–54] and experimental measurements [55,56]. Clearly, BOP calculations reproduce

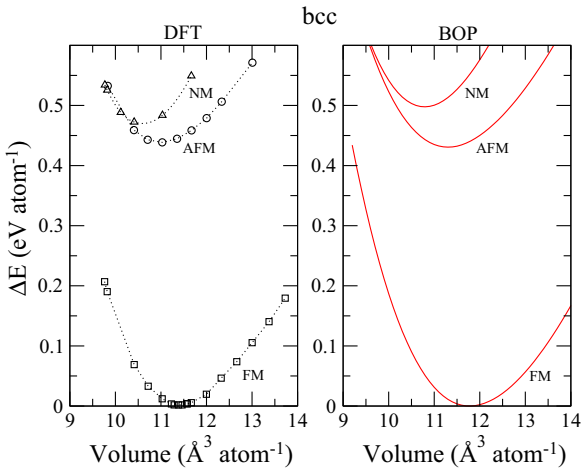

FIG. 2. Comparison of energies of different magnetic states in bcc lattice of iron relative to that of the equilibrium FM bcc lattice, plotted as dependences on the volume per atom. The DFT results are taken from Ref. [50].

TABLE II. Formation energies of vacancies (E_{vac}), formation energies of nearest neighbor (NN) and second nearest neighbor (2NN) divacancies (E_{divac}), and migration energies of vacancies (E_{mig}) calculated using the developed BOP and DFT and measured experimentally. Units are in eV.

	BOP	DFT	Experiment
E_{vac}	1.99	1.95–2.15[a,b]	1.6–2.2[g,h]
E_{divac} (NN)	3.51	3.85–4.08[c,d]	
E_{divac}(2NN)	3.61	3.83–4.01[c,d]	
E_{mig}	1.03	0.64–0.67[b,c,e,f]	0.55[g]

[a]Reference [51].
[b]Reference [52].
[c]Reference [53].
[d]Reference [54].
[e]Reference [57].
[f]Reference [58].
[g]Reference [55].
[h]Reference [56].

very well the formation energies of both vacancies and divacancies found in DFT calculations and experiments. Table II also contains the vacancy migration energy evaluated using the nudged elastic band (NEB) method [57]. In this case, the agreement with DFT calculations is only tentative but the important point is the comparison with the migration energy of interstitials discussed below.

C. Self-interstitial atoms

Based on the crystallography and symmetry of the bcc lattice, Johnson [5] proposed six possible configurations of SIAs: ⟨111⟩ dumbbell, ⟨111⟩ crowdion, ⟨110⟩ dumbbell, tetrahedral interstitial, ⟨100⟩ dumbbell, and octahedral interstitial. These configurations were used as the starting configuration in the relaxation calculations determining their final configurations and corresponding energies. The calculations were always started with the supercell composed of $4 \times 4 \times 4$ ideal bcc lattice unit cells with the equilibrium lattice parameter containing one SIA; the number of atoms in the supercell was 129. The periodic boundary conditions were applied in all three dimensions. The energy was then minimized with respect to both the positions of atoms using a steepest descent method and the volume of the supercell. The latter allows for the volume expansion/contraction associated with SIAs.

In starting configurations, the separations between the interstitial atoms and other atoms of the ideal lattice (or the separations between interstitial atoms) is often much smaller than the nearest neighbor spacing in the ideal lattice. This is seen in Table III, which summarizes the minimum interatomic separations, R^0_{min}, found in each unrelaxed SIA configurations. These separations range from 0.5–0.7 of the first nearest neighbor spacing in the ideal bcc lattice.

Formation energies of SIAs calculated using the developed BOP and using a DFT method [53], respectively, are presented in Table IV together with minimum interatomic separations, R_{min}, in the relaxed structures obtained using the BOP. Formation energies of ⟨111⟩ dumbbell and ⟨111⟩ crowdion were always found to be within the numerical errors the same and are not, therefore, presented separately. Relaxations generally lead to an increase of the minimum interatomic separations associated with SIAs, which, presumably, results from the expansions in their vicinity as can be expected.

TABLE III. The minimum interatomic separations, R^0_{min}, in the units of the first nearest neighbor spacing of the ideal bcc lattice (D), in the unrelaxed configurations of SIAs.

	⟨111⟩ dumbbell	⟨111⟩ crowdion	⟨110⟩ dumbbell
R^0_{min} (D)	0.567	0.500	0.693
	Tetrahedral interstitial	⟨100⟩ dumbbell	Octahedral interstitial
R^0_{min} (D)	0.645	0.722	0.577

The formation energies of SIAs found using the developed BOP are close to those found in DFT calculations [53]. The most important is that the configuration with the lowest formation energy is the ⟨110⟩ dumbbell, as predicted by DFT calculations. In contrast, in NM transition metals DFT calculations predict the lowest energy structure to be the ⟨111⟩ dumbbell [51]. Liu *et al.* [25] employed a TB model enhanced by the Stoner model of magnetism, and their results qualitatively reproduce prediction of DFT calculations, in particular the order of formation energies for various structures of SIAs. This suggests that it is the magnetism that is responsible for the lowest energy interstitial configuration in Fe to be different than in NM bcc transition metals. The constructed BOP that includes the magnetism in the same way clearly leads to the same finding for the lowest energy structure of SIAs. Additionally, the order of increasing formation energies with different configurations found by BOP is the same as that found using DFT.

In order to further demonstrate that it is the magnetism that governs the structure and energy of SIAs in bcc iron, we removed E^{mag} from evaluation of the cohesive energy while keeping E^{cov} the same and readjusting E^{rep} so as to reproduce the five fitting parameters as in the developed BOP. For this BOP that does not contain magnetism, the lowest energy configuration was found to be the ⟨111⟩ dumbbell with the energy of 1.22 eV, while the ⟨110⟩ dumbbell has appreciably

TABLE IV. Formation energies of SIAs (eV) together with minimum separations of atoms, R_{min}, in the structures relaxed using the BOP. In the calculations of R_{min}, only atomic relaxation was carried out without any total volume relaxation.

	Formation energies (eV)		
	BOP	DFT[a]	R_{min} (D)
⟨111⟩ dumbbell	4.22	4.61	0.801
⟨110⟩ dumbbell	3.87	3.93	0.813
Tetrahedral interstitial	4.24	4.32	0.836
⟨100⟩ dumbbell	4.44	5.05	0.797
Octahedral interstitial	5.05	5.21	0.817

[a]Ref. [53].

higher energy 2.14 eV. Thus, the lowest energy structure for NM iron is the same as in all NM transition metals.

Using the NEB method, the migration energy of the [110] dumbbell between two nearest positions along the [110] direction was found to be 0.28 eV. The DFT calculations give 0.34 eV [58], and the experimental values are in the range 0.27–0.33 eV [59]. Again, the agreement between BOP calculations, experiments, and DFT calculations is very good. However, the most important result is that the migration energy of SIAs is about a quarter of the migration energy of vacancies. This implies that SIAs migrate much faster than vacancies, which is a well-known phenomenon in irradiated materials in which vacancies and interstitials annihilate only partially and a surplus of vacancies ensues [60,61].

D. Transformation paths

The transformation paths studied connect the bcc lattice with fcc, simple cubic (sc), hcp, and body centered tetragonal (bct) structures via continuously distorted configurations. The four paths investigated are tetragonal, trigonal, hexagonal, and orthorhombic. The tetragonal path, also known as the Bain path [62], corresponds to extending the lattice along the [001] direction while keeping the volume per atom fixed. On the trigonal path, the lattice is deformed by extending along the [111] direction while keeping the volume per atom fixed. During the orthorhombic path, the lattice is deformed by extending in the [001] direction while compressing in the [110] direction. The hexagonal path is qualitatively different from the previous three paths in that it does not correspond only to a homogeneous straining but to straining accompanied by simultaneous shuffling of alternative close packed atomic planes in opposite directions; these shuffles are linearly coupled to the strain. A rigorous definition of tetragonal, trigonal, and hexagonal paths, using the Lagrange strain tensor, is found in Ref. [46], and the orthorhombic path is defined in the same way in Ref. [31].

All four paths can be characterized by one parameter p. We calculated for these paths the energy as a function of p using both the developed BOP and spin polarized DFT as included in the Vienna *Ab initio* Simulation Package (VASP) code [63–65]. Results of these calculations are presented in Fig. 3. In general, the agreement between BOP and DFT calculations is very

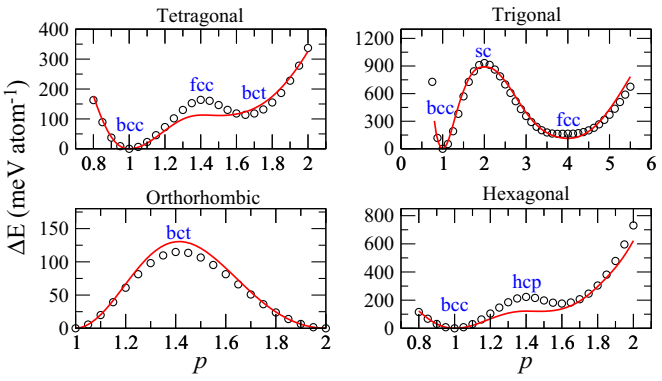

FIG. 3. Deformation paths calculated using the constructed BOP (full curves) and DFT (circles). The positions (values of p) for which the structures are bcc, fcc, sc, bct, and hcp are marked.

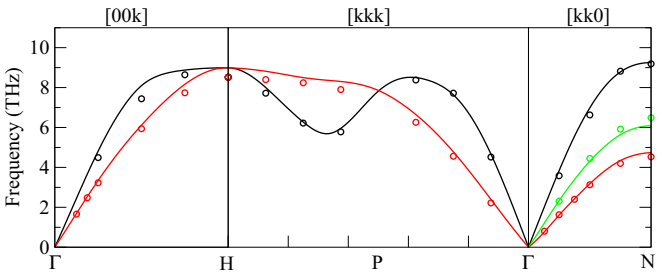

FIG. 4. Phonon dispersion curves. Lines: calculations using the constructed BOP. Circles: experimental data from Ref. [67]. The black color corresponds to the longitudinal mode L, red to the transversal modes T and T1, and green to the transversal mode T2 for both the BOP results and the experimental data.

good, which demonstrates that the BOP describes with a good precision the interaction between atoms for structures that deviate very significantly from the ideal bcc lattice.

E. Phonon dispersions

The phonon dispersion curves for the equilibrium bcc lattice of iron were calculated using the constructed BOP by employing the frozen phonons method [66]. The calculations were done for Γ-H, H-P-Γ, and Γ-N cross sections of the Brillouin zone. The results, compared with the available experimental data [67], are presented in Fig. 4. The calculated dispersion curves are in an excellent agreement with experiments. They do not show any tendency towards soft phonons, which would indicate possible instabilities. This demonstrates the robustness of the developed BOP since no information associated with the phonon spectra (besides elastic moduli) has been included into the fitting database when developing the BOP.

F. Core structure and glide of ½⟨111⟩ screw dislocations

It is now firmly established that the plastic deformation of pure single crystals of all bcc metals is governed by ½⟨111⟩ screw dislocations that possess nonplanar cores (for reviews see Refs. [48], [49], and [68]). The most important features of these cores can be assessed using the concept of γ surfaces that are plots of energies of single layer generalized stacking faults formed by displacing relative to each other two parts of a crystal cut along a crystallographic plane. When calculating a γ surface, the relaxation of atomic planes perpendicular to the plane of the fault has to be carried out. Such calculations were made for many bcc crystals using a variety of interatomic potentials as well as DFT. For bcc iron, the latter was used, for example, in Refs. [69–71]. In all these studies, γ surfaces do not display any minima that would indicate existence of metastable stacking faults. Calculations employing the constructed BOP for bcc iron give the same results. Comparison between the BOP and DFT [69] calculated [111] cross-sections of γ surfaces for the $(\bar{1}01)$ plane, shown in Fig. 5, demonstrates that the two calculations are very close to each other even numerically. Nonexistence of metastable stacking faults is, of course, a general characteristic of all bcc metals [68].

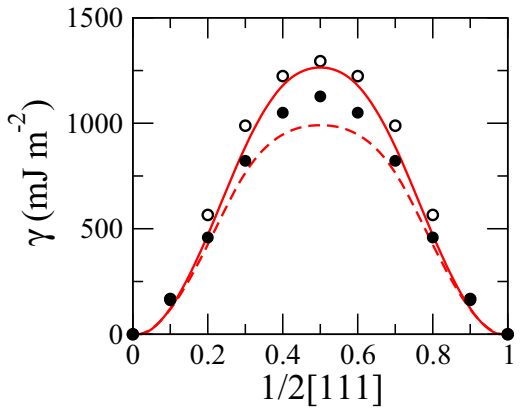

FIG. 5. [111] cross-sections of γ surfaces for the $(\bar{1}01)$ plane calculated by BOP and DFT. Lines: BOP; dashed and solid lines correspond to calculations with and without the relaxation perpendicular to the $(\bar{1}01)$ plane, respectively. Filled and open circles are results of DFT calculations (Ref. [69]) with and without the relaxation perpendicular to the $(\bar{1}01)$ plane, respectively.

The core structure of the $1/2[111]$ screw dislocation was computer modeled using the constructed BOP in the same way as in a number of previous studies (see, for example, Ref. [72]). The relaxed block of atoms consisted of three consecutive, periodically repeated, (111) planes of the bcc lattice. It comprised two regions: An active region in the center surrounded by an inert region. The dislocation was centered in the active region in which all the atoms are relaxed using the steepest decent molecular statics method, while the atoms in the inert region are fixed but displaced away from the ideal bcc lattice in accordance with the elastic anisotropic displacement field of the dislocation studied. This arrangement corresponds to the simulation of an infinitely long $1/2[111]$ screw dislocation located in the bulk of the material [73]. Within the core, the largest displacements in the [111] direction are confined to three intersecting $\{101\}$ planes of the [111] zone. The core structure is invariant with respect to the [111] threefold screw axis and also with respect to the $[\bar{1}01]$ diad (reflection in the (111) plane followed by reflection in the $(\bar{1}2\bar{1})$ plane). This core structure is unique and called nondegenerate. (More details about the depiction of the core structure can be found in the review [68].) The same core structure was found for bcc iron in several DFT studies [69,74–76]. In fact, the same core structure was also found in NM bcc metals studied using DFT and/or BOPs (for references, see Refs. [72] and [77]), and thus the principal aspects of the structure of the core of $1/2\langle 111\rangle$ screw dislocations are the same in the bcc iron as in NM bcc transition metals.

The motion of the dislocation under the effect of an applied stress at 0 K was investigated as follows. We applied the chosen stress to the block with the relaxed atomic configuration of the $1/2[111]$ screw dislocation by imposing on all the atoms of the block the displacement evaluated for the given applied stress tensor via the corresponding strain tensor using the anisotropic Hook's law. The level of the applied stress always started well below the stress at which the dislocation moved. The stress was then increased incrementally, and at each stress level the atoms in the active region were fully relaxed as in the unstressed case. The stress level keeps increasing until the dislocation starts to glide at a critical stress.

TABLE V. Glide planes of the $1/2[111]$ screw dislocation for pure shear stress applied in the [111] direction in different MRSSPs and tension/compression applied for eight different loading axes. In each case, the MRSSP is characterized by the angle χ.

	Pure shear	Tension		Compression	
χ (deg)	Glide plane	Axis	Glide plane	Axis	Glide plane
−26.33	$(\bar{1}01)$	$[0\,1\,14]$	$(\bar{1}01)$	$[\bar{5}\,8\,9]$	$(\bar{1}01)$ and $(\bar{1}10)$
−19.11	$(\bar{1}01)$	$[\bar{1}\,6\,34]$	$(\bar{1}01)$	$[\bar{8}\,20\,27]$	$(\bar{1}01)$
−8.95	$(\bar{1}01)$	$[\bar{1}\,3\,10]$	$(\bar{1}01)$	$[\bar{5}\,9\,17]$	$(\bar{1}01)$ and $(\bar{1}10)$
0.00	$(\bar{1}01)$	$[\bar{2}\,3\,8]$	$(\bar{1}01)$	$[0\,1\,2]$	$(\bar{1}01)$
0.00	–	$[0\,1\,2]$	$(\bar{1}01)$	$[\bar{2}\,3\,8]$	$(\bar{1}01)$ and $(\bar{1}10)$
8.95	$(\bar{1}01)$	$[\bar{5}\,9\,17]$	$(\bar{1}01)$	$[\bar{1}\,3\,10]$	$(\bar{1}01)$
19.11	$(\bar{1}01)$	$[\bar{8}\,20\,27]$	$(\bar{1}01)$	$[\bar{1}\,6\,34]$	$(\bar{1}01)$
26.33	$(\bar{1}01)$	$[\bar{5}\,8\,9]$	$(\bar{1}01)$	$[0\,1\,14]$	$(\bar{1}01)$

The stresses we imposed were pure shear stress in the direction of the Burgers vector in several planes, called maximum resolved shear stress planes (MRSSPs), making an angle χ with the $(\bar{1}01)$ plane and tensile/compressive stresses for a number of loading axes within the standard stereographic triangle with the corners [001], [011], and $[\bar{1}11]$. In all cases, the $\{101\}$ plane most highly stressed by the shear in the [111] direction was the $(\bar{1}01)$ plane. The shear stress driving the dislocation attains in each case a maximum at a MRSSP making an angle χ with the $(\bar{1}01)$ plane. The corresponding shear stress at which the dislocation starts to move is called the critical resolved shear stress (CRSS). For crystallographic reasons, all nonequivalent angles χ are in the range $-30^\circ \leqslant \chi \leqslant +30^\circ$. The procedure of stress applications is described in more detail in Ref. [72].

Table V summarizes the glide planes of the $1/2[111]$ screw dislocation found when applying the pure shear stress in the [111] direction in different MRSSPs and tension/compression for eight different loading axes. The dependence of the CRSS (normalized by C_{44}) on the angle χ is presented in Fig. 6. Similarly, as for NM bcc transition metals [72,77], the

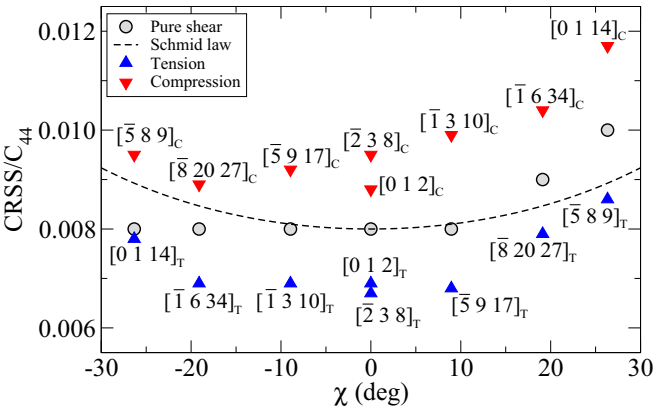

FIG. 6. The dependence of the CRSS on χ calculated using the developed BOP for the bcc iron. Loading axes are shown and marked by subscripts T and C for tension and compression, respectively.

Schmid law breaks down for all loadings, and the orientation dependence of the CRSS always displays the asymmetry between twinning ($\chi < 0$) and antitwinning ($\chi > 0$) sense of shearing. Moreover, there is also a significant difference between tension and compression for a fixed χ that cannot be related just to the effect of pure shear in the direction of the Burgers vector, and it was shown in Refs. [72] and [77] that the shear stress components perpendicular to the Burgers vector are likely to play an important role in this asymmetry [78]. Hence, the CRSS versus χ dependence and the asymmetries this dependence demonstrates are in the bcc iron very similar to those in NM bcc transition metals [30,31,72,77]. However, a noticeable difference is found in the case of the slip planes. In NM bcc transition metals, the slip planes are $\{101\}$ planes of the [111] zone that may but need not be most highly stressed [72,77], depending on loading conditions. In contrast, for bcc iron the slip plane is almost always the $(\bar{1}01)$ plane, which is the most highly stressed $\{101\}$ plane. Only for some orientations of the compressive axis, the combination of $(\bar{1}01)$ and $(\bar{1}10)$ is found, which represents effectively the slip along the $(\bar{2}11)$ plane sheared in the twinning sense.

The general experimental finding is that, in single crystals of bcc iron, the preferred slip planes at low temperatures are $\{101\}$ planes and, just like in NM transition metals, the CRSS always shows a significant twinning-antitwinning asymmetry (see, for example, Refs. [79–84]). Moreover, for some orientations of the loading axes, when $\chi < 0$, the slip plane for the [111] slip direction is the $(\bar{2}11)$ plane. Our calculations of the glide of ½[111] screw dislocation fully support these experimental observations. Furthermore, the anomalous slip, i.e., the slip on a system with a very low Schmid factor, has been observed to various extent, sometimes even as dominating, in NM bcc transition metals deformed at cryogenic temperatures [85–87]. This aspect of the low temperature behavior is supported by recent atomistic calculations of the glide of the screw dislocation in NM bcc transition metals [77]. However, calculations of the glide of ½[111] screw dislocation in the bcc iron do not indicate existence of such slip. Indeed, the anomalous slip has never been observed in the bcc iron. This demonstrates that atomistic studies using the developed BOP for the bcc iron are correctly reproducing the experimentally observed dislocation behavior.

IV. CONCLUSIONS

In this paper, the BOP for FM bcc iron (α-iron) was developed that comprises the most important aspects of bonding in this important metal. In the attractive part of the cohesive energy, it is the mixed nearly free electron and covalent bonding, the former mainly due to s electrons and the latter owing to a partially filled d band. The ferromagnetism, which is essential for the stability of the bcc structure [4], is taken into account aptly within the Stoner model of itinerant magnetism [14,15] and, importantly, the repulsive part of the cohesive energy, albeit principally empirical, contains an environmentally dependent term that is essential for exact reproduction of the elastic moduli. While only dd bonding is considered explicitly, the influence of s electrons is included implicitly via screening of dd bonds [32]. Neither the influence of s electrons on dd bonds nor the environmental dependence of the repulsion was included in the earlier development of the BOP for the bcc iron [13]. Naturally, none of these aspects is captured by any potentials that include only central-force interactions even if these potentials have a many-body character, as in EAM or F-S potentials.

The testing of the transferability of the developed BOP to atomic environments that are significantly different from those of the ideal bcc lattice, compared either with experiments or analogous DFT calculations, shows indubitably that the potential can be employed with high confidence in large-scale atomistic computer modeling of crystals with defects. The most important aspect is that its applicability extends from simplest point defects to large extended defects. Thus, it is possible to model the glide of individual dislocations as well as their mutual interactions and interactions with interfaces equally well as with localized defects such as interstitials and vacancies. This implies, for example, that the developed BOP may be employed equally in studies of plastic deformation, grain boundary migration or sliding, effects of radiation damage associated with formation and movement of SIAs and vacancies, and other defects in the crystalline structure. While no empirical or semiempirical potential can be entirely all-embracing and some limits of its applicability always exist, the present paper suggests that the applicability of the developed BOP for bcc iron is, indeed, very wide-ranging.

ACKNOWLEDGMENTS

The authors would like to thank Dr. Nguyen-Manh for illuminating discussions, in particular on the magnetic contribution to the cohesive energy. The research was supported by the US Department of Energy, Office of Basic Energy Sciences, Grant No. DEPG02-98ER45702 (Y.-S.L. and V.V.) and the Helmholtz Portfolio Project Energy Materials EMR (M.M.). This paper was partially supported (M.M.) by the EU project "Z-Ultra" funded by FP7 under NMP.2012.2.2-3—Advanced materials for high-temperature power generation call with Grant Agreement No. 309916.

APPENDIX A: SCREENED BIs

In Eq. (3),

$$\beta_\tau(R_{ij}) = \beta_\tau(R_0)\exp\left(\frac{R_0}{R_c} - \frac{R_{ij}}{R_c}\right). \tag{A1}$$

This is a simplified form of the more general Goodwin, Skinner, and Pettifor (GSP) [88] form that was used in previous developments of BOPs. Both R_0 and R_c, as well as $\beta_\tau(R_0)$, are adjustable parameters used when fitting the R dependence of the BIs shown in Fig. 1. The screening function is taken as

$$S_\tau^{ij} = \frac{\left(c_1^{ij}\right)_\tau - \left(\bar{\mu}_2^{ij}\right)_\tau}{1 + O_\tau^2(R_{ij}) - 2\left(\bar{\mu}_2^{ij}\right)_\tau}, \tag{A2}$$

which is a simplified form of S_τ^{ij} derived in Ref. [32]. The $O_\tau(R_{ij})$ is the dd overlap integral of the type τ between atoms i and j; it is assumed to have the same functional form as β_τ. The $O_\tau(R_0)$ is then one of the adjustable parameters used to reproduce both the environmental (discontinuities) and R dependence of the BIs of the dd type. The $(c_1^{ij})_\tau$ is

TABLE VI. Parameters entering equations for screened bond integrals for bcc Fe. For all four BIs ($dd\sigma$, $dd\pi$, $dd\delta$, and $sd\sigma$), $R_0 = 2.4825$ Å, $R_1^{\mathrm{BI}} = 2.6$ Å, and $R_{\mathrm{cut}}^{\mathrm{BI}} = 4.0$ Å. Units of $\beta_\tau(R_0)$ and $O_\tau(R_0)$ are eV; R_c is in Å.

	$\beta_\tau(R_0)$	$O_\tau(R_0)$	R_c
$dd\sigma$	−0.620	0.040	0.71
$dd\pi$	0.410	−0.030	0.47
$dd\delta$	−0.062	0.020	0.31
$sd\sigma$	0.845	−0.045	0.71

the contribution of the interference between atoms i and j that results from the electrons hopping between d orbitals on atoms i and j through the s orbital centered on a neighboring atom k. Following Ref. [32], it is

$$\begin{aligned}\left(c_1^{ij}\right)_\tau = \sum_{k\neq i,j} \frac{(1+\delta_{\tau 0})}{4\beta_\tau(R_{ij})}\{&[\beta_{ds\sigma}(R_{ik})O_{sd\sigma}(R_{kj}) \\ &+ O_{ds\sigma}(R_{ik})\beta_{sd\sigma}(R_{kj})]g_\tau(\theta_{jik})g_\tau(-\theta_{ijk}) \\ &- \beta_{ds\sigma}(R_{ik})O_{sd\sigma}(R_{ki})O_\tau(R_{ij})g_\tau^2(\theta_{jik}) \\ &- O_\tau(R_{ij})O_{ds\sigma}(R_{jk})\beta_{sd\sigma}(R_{kj})g_\tau^2(\theta_{ijk})\},\end{aligned}$$

where $\delta_{\tau 0}$ is 0 when $\tau = \pi$ or δ and 1 when $\tau = \sigma$. The functional dependence on R of the BI $\beta_{sd\sigma}$ is determined from DFT calculation similar to that used for dd integrals, but it is further modified when fitting dd BIs. The overlap integral $O_{sd\sigma}$ is again assumed to have the same functional dependence on R as $\beta_{sd\sigma}$, and $O_{sd\sigma}(R_0)$ is then used as an adjustable parameter when fitting dd BIs. Moreover, the BI $\beta_{ds\sigma}$ and the overlap integral $O_{ds\sigma}$ are assumed to be the same as $\beta_{sd\sigma}$ and $O_{sd\sigma}$, respectively. The screening function of BIs not only contains a many-body character, but it also depends explicitly on bond angles θ_{ijk} and θ_{jik} via angular functions [32] $g_\sigma(\theta) = \frac{1}{4}(1 + 3\cos 2\theta)$, $g_\pi(\theta) = \frac{\sqrt{3}}{2}\sin 2\theta$, and $g_\delta(\theta) = \frac{\sqrt{3}}{4}(1 - \cos 2\theta)$. The $(\bar{\mu}_2^{ij})_\tau$ is the average second moment contribution, and it is [32]

$$\begin{aligned}\left(\bar{\mu}_2^{ij}\right)_\tau = O_\tau^2(R_{ij}) + \sum_{k\neq i,j}\frac{(1+\delta_{\tau 0})}{4}\big[&O_{ds\sigma}^2(R_{ik})g_\tau^2(\theta_{jik}) \\ &+ O_{ds\sigma}^2(R_{jk})g_\tau^2(\theta_{ijk})\big].\end{aligned}$$

The parameters $O_\tau(R_0)$ and $O_{sd\sigma}(R_0)$ in the overlap integrals, together with a modification of parameters in $\beta_\tau(R)$ and $\beta_{sd\sigma}(R)$ [all represented by the functional form of the type as in Eq. (A1)], are used to reproduce the R dependence and the environmental dependence (discontinuities) of the DFT determined BIs of dd type shown in Fig. 1. The solid lines in this figure show BIs calculated analytically using Eq. (3). Parameters entering Eq. (A1) and quantities entering the screening function given by Eq. (A2) are summarized in Table VI.

TABLE VII. Experimental values [89,90] to which the BOP is fitted. The lattice parameter (a) is in Å, the cohesive energy (E^{coh}) in eV, and elastic moduli in 10^{11} Pa.

a	E^{coh}	C_{11}	C_{12}	C_{44}
2.866	4.28	2.431	1.381	1.219

TABLE VIII. Parameters used in the environment dependent repulsion (E^{env}), given by equations (B1) and (B2), when R_{ij} is in units of the lattice parameter a. A is in eV; μ, g, and ν are dimensionless; R_s is in units of a; R_1^{rep} and $R_{\mathrm{cut}}^{\mathrm{rep}}$ are in Å.

A	μ	g	ν	R_s	R_1^{rep}	$R_{\mathrm{cut}}^{\mathrm{rep}}$
1.297×10^2	7.0	20.0	6.0	0.52	3.0	4.0

In order to ensure that no nonphysical discontinuity occurs when calculating the energy and forces for a finite range of R values, it is important that the R dependence of BIs converges smoothly to zero at a cutoff distance $R_{\mathrm{cut}}^{\mathrm{BI}}$. This is achieved by replacing $\beta_\tau(R)$ by a fifth-order polynomial when $R_1^{\mathrm{BI}} < R < R_{\mathrm{cut}}^{\mathrm{BI}}$. The coefficients of this polynomial are determined such that $\beta_\tau(R)$ and the polynomial have the same values and the same first and second derivatives at $R = R_1^{\mathrm{BI}}$ and that at $R = R_{\mathrm{cut}}^{\mathrm{BI}}$ the value, the first derivative, and the second derivative of the polynomial become zero; $R_{\mathrm{cut}}^{\mathrm{BI}}$ is between the second and third nearest neighbors, which is a sufficient interaction range. The values of R_1^{BI} and $R_{\mathrm{cut}}^{\mathrm{BI}}$ are chosen carefully to avoid any unphysical bump of the polynomial in the interval $R_1^{\mathrm{BI}} < R < R_{\mathrm{cut}}^{\mathrm{BI}}$, and their values are also presented in the caption of Table VI.

APPENDIX B: REPULSIVE PART OF THE COHESIVE ENERGY: Eq. (7)

The functional form for the environment dependent repulsion (for more details see Ref. [26]) is

$$E^{\mathrm{env}} = \frac{1}{2}\sum_{i,j\neq i} A\exp(-\mu R_{ij})e^{-(\lambda_i+\lambda_j)(R_{ij}-R_s)}, \tag{B1}$$

with

$$\lambda_i = \sum_{k\neq i} g\exp(-\nu R_{ik}), \tag{B2}$$

where A, μ, g, ν, and R_s are adjustable parameters. The pairwise repulsion

$$E^{\mathrm{pair}} = \frac{1}{2}\sum_{i,j\neq i}\Phi(R_{ij}), \tag{B3}$$

where $\Phi(R_{ij})$ is a pair potential taken in the form

$$\Phi(R_{ij}) = \sum_{k=0}^{4} B_k(R_k - R_{ij})^3 H(R_k - R_{ij}), \tag{B4}$$

TABLE IX. Parameters used in the pair potential (Φ), given by Eq. (B4), when R_{ij} is in Å. R_k is in Å; B_k is in eV Å^{-3}.

k	R_k	B_k
0	2.23	30.0
1	2.75	−0.972 681 58
2	2.90	2.516 912 64
3	3.50	0.693 543 45
4	3.80	−0.412 698 08

where B_k and R_k are adjustable parameters, H is the Heaviside step function, and R_4 is the cutoff of the pair potential. For computational reasons, E^{env} needs to be cut off at a certain interatomic distance, $R_{\text{cut}}^{\text{rep}}$, which is chosen to be in the vicinity of the third nearest neighbors. This is achieved by replacing $A\exp(-\mu R)$ in Eq. (B1) and $g\exp(-\nu R)$ in Eq. (B2) by fifth-order polynomials when $R_1^{\text{rep}} < R < R_{\text{cut}}^{\text{rep}}$; the coefficients of these polynomials are determined such that their values and first and second derivatives are continuous at $R = R_1^{\text{rep}}$ with $A\exp(-\mu R)$ and $g\exp(-\nu R)$, respectively, and zero at $R = R_{\text{cut}}^{\text{rep}}$. The R_1^{rep} is chosen such that there are no unphysical bumps occurring in the polynomials in the range $R_1^{\text{rep}} < R < R_{\text{cut}}^{\text{rep}}$. The adjustable parameters in both E^{env} and E^{pair} are determined such that the resulting BOP reproduces the experimental values of the lattice constant (a), cohesive energy (E^{coh}), and three elastic constants (C_{11}, C_{12}, and C_{44}) of the equilibrium bcc phase. These are summarized in Table VII. Parameters entering E^{env} are summarized in Table VIII, and those entering the pairwise repulsion are summarized in Table IX.

[1] R. O. Jones, Rev. Mod. Phys. **87**, 897 (2015).
[2] D. G. Pettifor, Phys. Educ. **32**, 164 (1997).
[3] D. G. Pettifor, M. Aoki, P. Gumbsch, A. P. Horsfield, D. Nguyen-Manh, and V. Vitek, Mater. Sci. Eng. A **192–193**, 24 (1995).
[4] H. Hasegawa and D. G. Pettifor, Phys. Rev. Lett. **50**, 130 (1983).
[5] R. A. Johnson, Phys. Rev. **134**, A1329 (1964).
[6] M. I. Mendelev, S. Han, D. J. Srolovitz, G. J. Ackland, D. Y. Sun, and M. Asta, Philos. Mag. **83**, 3977 (2003).
[7] P. A. Gordon, T. Neeraj, and M. I. Mendelev, Philos. Mag. **91**, 3931 (2011).
[8] M. I. Baskes, Phys. Rev. B **46**, 2727 (1992).
[9] M. Müller, P. Erhart, and K. Albe, J. Phys.: Condens. Matter **19**, 326220 (2007).
[10] J. A. Harrison, M. Fallet, K. E. Ryan, B. L. Mooney, M. T. Knippenberg, and J. D. Schall, Model. Simul. Mater. Sci. Eng. **23**, 074003 (2015).
[11] J. Tersoff, Phys. Rev. B **38**, 9902 (1988).
[12] S. L. Dudarev and P. M. Derlet, J. Phys.: Condens. Matter **17**, 7097 (2005).
[13] M. Mrovec, D. Nguyen-Manh, C. Elsässer, and P. Gumbsch, Phys. Rev. Lett. **106**, 246402 (2011).
[14] E. C. Stoner, Proc. R. Soc. Lond. A **165**, 372 (1938).
[15] E. C. Stoner, Proc. R. Soc. Lond. A **169**, 339 (1939).
[16] D. G. Pettifor, Phys. Rev. Lett. **63**, 2480 (1989).
[17] A. P. Horsfield, A. M. Bratkovsky, M. Fearn, D. G. Pettifor, and M. Aoki, Phys. Rev. B **53**, 12694 (1996).
[18] A. P. Horsfield, A. M. Bratkovsky, D. G. Pettifor, and M. Aoki, Phys. Rev. B **53**, 1656 (1996).
[19] M. W. Finnis, Prog. Mater. Sci. **52**, 133 (2007).
[20] M. Aoki, D. Nguyen-Manh, D. G. Pettifor, and V. Vitek, Prog. Mater. Sci. **52**, 154 (2007).
[21] T. Hammerschmidt and R. Drautz, in *Multiscale Simulation Methods in Molecular Sciences*, edited by J. Grotendorst *et al.*, (Institute for Advanced Simulation, Forschungszentrum Jülich, NIC Series, Jülich, 2009), p. 229.
[22] T. Hammerschmidt, R. Drautz, and D. G. Pettifor, Int. J. Mater. Res. **100**, 1479 (2009).
[23] L. Pastewka, M. Mrovec, M. Moseler, and P. Gumbsch, MRS Bull. **37**, 493 (2012).
[24] R. Drautz, T. Hammerschmidt, M. Čák, and D. G. Pettifor, Model. Simul. Mater. Sci. Eng. **23**, 074004 (2015).
[25] G. Q. Liu, D. Nguyen-Manh, B. G. Liu, and D. G. Pettifor, Phys. Rev. B **71**, 174115 (2005).
[26] Y.-S. Lin, M. Mrovec, and V. Vitek, Model. Simul. Mater. Sci. Eng. **22**, 034002 (2014).
[27] J. C. Slater and G. F. Koster, Phys. Rev. **94**, 1498 (1954).
[28] A. Urban, M. Reese, M. Mrovec, C. Elsässer, and B. Meyer, Phys. Rev. B **84**, 155119 (2011).
[29] G. K. H. Madsen, E. J. McEniry, and R. Drautz, Phys. Rev. B **83**, 184119 (2011).
[30] M. Mrovec, D. Nguyen-Manh, D. G. Pettifor, and V. Vitek, Phys. Rev. B **69**, 094115 (2004).
[31] M. Mrovec, R. Gröger, A. G. Bailey, D. Nguyen-Manh, C. Elsässer, and V. Vitek, Phys. Rev. B **75**, 104119 (2007).
[32] D. Nguyen-Manh, D. G. Pettifor, and V. Vitek, Phys. Rev. Lett. **85**, 4136 (2000).
[33] In the earlier development of the BOP for iron [13], screening of BIs was not included.
[34] A. P. Horsfield and A. M. Bratkovsky, Phys. Rev. B **53**, 15381 (1996).
[35] F. Ducastelle and F. Cyrot-Lackmann, J. Phys. Chem. Solids **31**, 1295 (1970).
[36] P. Turchi and F. Ducastelle, in *The Recursion Method and Its Applications*, edited by D. G. Pettifor and D. L. Weaire (Springer, Berlin, 1985), p. 104.
[37] M. Aoki, Phys. Rev. Lett. **71**, 3842 (1993).
[38] M. Aoki and D. G. Pettifor, Int. J. Mod. Phys. B **7**, 299 (1993).
[39] A. P. Horsfield, P. D. Godwin, D. G. Pettifor, and A. P. Sutton, Phys. Rev. B **54**, 15773 (1996).
[40] M. Aoki and T. Kurokawa, J. Phys.: Condens. Matter **19**, 236228 (2007).
[41] D. G. Pettifor, J. Phys. F: Met. Phys. **8**, 219 (1978).
[42] M. Šob and V. Vitek, in *Stability of Materials: NATO Advanced Science Institute Series*, edited by A. Gonis, P. E. A. Turchi, and J. Kudrnovsky (Plenum Press, New York, 1996), p. 449.
[43] D. Nguyen-Manh, D. G. Pettifor, S. Znam, and V. Vitek, in *Tight-Binding Approach to Computational Materials Science*, edited by P. E. A. Turchi, A. Gonis, and L. Colombo (Materials Research Society, Pittsburgh, 1998), p. 353.
[44] R. P. Feynman, Phys. Rev. **56**, 340 (1939).
[45] P. Soin, A. P. Horsfield, and D. Nguyen-Manh, Comput. Phys. Commun. **182**, 1350 (2011).
[46] V. Paidar, L. G. Wang, M. Šob, and V. Vitek, Model. Simul. Mater. Sci. Eng. **7**, 369 (1999).
[47] T. Kana, M. Šob, and V. Vitek, Intermetallics **19**, 919 (2011).
[48] J. W. Christian, Metall. Trans. A **14**, 1237 (1983).
[49] M. S. Duesbery, in *Dislocations in Solids*, edited by F. R. N. Nabarro (Elsevier, Amsterdam, 1989), p. 67.
[50] H. C. Herper, E. Hoffmann, and P. Entel, Phys. Rev. B **60**, 3839 (1999).
[51] D. Nguyen-Manh, A. P. Horsfield, and S. L. Dudarev, Phys. Rev. B **73**, 020101(R) (2006).

[52] C. Domain and C. S. Becquart, Phys. Rev. B **65**, 024103 (2002).
[53] P. M. Derlet, D. Nguyen-Manh, and S. L. Dudarev, Phys. Rev. B **76**, 054107 (2007).
[54] C. J. Forst, J. Slycke, K. J. Van Vliet, and S. Yip, Phys. Rev. Lett. **96**, 175501 (2006).
[55] H. Ulmeier, in *Landolt-Börnstein New Series, Group III*, edited by H. Ullmeir (Springer-Verlag, Berlin, 1991).
[56] L. Deschepper, D. Segers, L. Dorikensvanpraet, M. Dorikens, G. Knuyt, L. M. Stals, and P. Moser, Phys. Rev. B **27**, 5257 (1983).
[57] C. C. Fu, F. Willaime, and P. Ordejon, Phys. Rev. Lett. **92**, 175503 (2004).
[58] F. Willaime, C. C. Fu, M. C. Marinica, and J. Dalla Torre, Nucl. Instrum. Methods Phys. Res., Sec. B **228**, 92 (2005).
[59] H. Schultz, Atomic Defects in Metals, Landolt-Börnstein NS III/25, 115 (1991).
[60] R. Bullough, B. L. Eyre, and G. L. Kulcinski, J. Nucl. Mater. **68**, 168 (1977).
[61] N. I. Budylkin, E. G. Mironova, V. M. Chernov, V. A. Krasnoselov, S. I. Porollo, and F. A. Garner, J. Nucl. Mater. **375**, 359 (2008).
[62] E. C. Bain, Trans. AIME **70**, 25 (1924).
[63] G. Kresse and J. Hafner, Phys. Rev. B **47**, 558 (1993).
[64] G. Kresse and J. Furthmüller, Comput. Mater. Sci. **6**, 15 (1996).
[65] G. Kresse and J. Furthmüller, Phys. Rev. B **54**, 11169 (1996).
[66] K. Kunc, *Electronic Structure Dynamics and Quantum Structure Properties of Condensed Matter* (Plenum Press, New York, 1985).
[67] B. N. Brockhouse, H. E. Abou-Helal, and E. D. Hallman, Solid State Commun. **5**, 211 (1967).
[68] V. Vitek and V. Paidar, in *Dislocations in Solids*, edited by J. P. Hirth (Elsevier, Amsterdam, 2008), p. 439.
[69] S. L. Frederiksen and K. W. Jacobsen, Philos. Mag. **83**, 365 (2003).
[70] L. Ventelon and F. Willaime, Philos. Mag. **90**, 1063 (2010).
[71] L. Dezerald, L. Ventelon, E. Clouet, C. Denoual, D. Rodney, and F. Willaime, Phys. Rev. B **91**, 019902 (2015).
[72] R. Gröger, A. G. Bailey, and V. Vitek, Acta Mater. **56**, 5401 (2008).
[73] The relaxation was always regarded as complete when the maximum force on any atom in the active region was less than 10^{-4} eV Å^{-1}. The validity of this condition was thoroughly tested by trying a variety of maximum forces. In all calculations, the active region contained 711 atoms, and the inert region 858 atoms. This size of the block had been used in earlier calculations [72] and tested to be large enough even when the dislocation starts to move under the effect of an applied stress.
[74] L. Ventelon and F. Willaime, J. Comput.-Aided Mater. Des. **14**, 85 (2007).
[75] L. Ventelon, F. Willaime, E. Clouet, and D. Rodney, Acta Mater. **61**, 3973 (2013).
[76] C. R. Weinberger, G. J. Tucker, and S. M. Foiles, Phys. Rev. B **87**, 054114 (2013).
[77] Y.-S. Lin, Ph.D. thesis, University of Pennsylvania, 2015.
[78] The magnitude of the CRSS is, similarly as in all the calculations for bcc metals, higher by a factor of two or three than what can be deduced from experiments at low temperatures. An explanation of this discrepancy was suggested in terms of the collective motion of many dislocations rather than of one dislocation in real crystals [91] and, alternatively, by the effect of zero vibrations at low temperatures [92]. Nevertheless, the source of this discrepancy found in all atomistic studies of dislocations is not yet fully understood.
[79] H. D. Nine, Philos. Mag. **26**, 1409 (1972).
[80] P. Vagnieux, P. Azou, and P. Bastien, C. R. Seances Acad. Sci., Ser. C **270**, 1635 (1970).
[81] W. A. Spitzig and A. S. Keh, Metal. Trans. **1**, 2751 (1970).
[82] Y. Aono, E. Kuramoto, and K. Kitajima, Reports of Research Institute for Applied Mechanics, Kyushu University **29**, 127 (1981).
[83] D. Brunner and J. Diehl, Z. Metallk. **83**, 828 (1992).
[84] C. Kahloun, L. T. Le, G. Monnet, M. H. Chavanne, E. Ait, and P. Franciosi, Acta Mater. **61**, 6453 (2013).
[85] C. J. Bolton and G. Taylor, Philos. Mag. **26**, 1359 (1972).
[86] G. Taylor, R. Bajaj, and O. N. Carlson, Philos. Mag. **28**, 1035 (1973).
[87] A. Seeger and W. Wasserbäch, Phys. Status Solidi A **189**, 27 (2002).
[88] L. Goodwin, A. J. Skinner, and D. G. Pettifor, Europhys. Lett. **9**, 701 (1989).
[89] C. Kittel, *Introduction to Solid State Physics* (Wiley, New York, 1996).
[90] J. A. Rayne and B. S. Chandrasekhar, Phys. Rev. **122**, 1714 (1961).
[91] R. Gröger and V. Vitek, Philos. Mag. Lett. **87**, 113 (2007).
[92] L. Proville, D. Rodney, and M. C. Marinica, Nat. Mater. **11**, 845 (2012).